Developing breakage models relating morphological data to the milling behaviour of flame synthesised titania particles

Casper Lindberg[a], Jethro Akroyd[a], Markus Kraft[a,b,*]

[a] *Department of Chemical Engineering and Biotechnology, University of Cambridge, New Museums Site, Pembroke Street, Cambridge CB2 3RA, United Kingdom*
[b] *School of Chemical and Biomedical Engineering, Nanyang Technological University, 62 Nanyang Drive, 637459, Singapore*

Abstract

A detailed population balance model is used to relate the reactor conditions of flame synthesised titanium dioxide particles to their milling behaviour. Breakage models are developed that utilise morphological data captured by a detailed particle model to relate the structure of aggregate particles to their size-reduction behaviour in the post-synthesis milling process. Simulations of a laboratory-scale hot wall reactor are consistent with experimental data and milling curves predicted by the breakage models exhibit features consistent with experimental observations. The selected breakage model considers the overall fractal structure of the aggregate particles as well as the neck size between neighbouring primary particles. Application of the model to particles produced under different reactor residence times and temperatures demonstrates that the model can be used to relate reactor conditions to the milling performance of titanium dioxide particles.

Keywords: Titania, population balance, breakage, milling

*Corresponding author
Email address: mk306@cam.ac.uk (Markus Kraft)

1. Introduction

Titanium dioxide (titania, TiO_2) particles are an important industrial product. The functionality of the product is strongly influenced by the size, shape, morphology and crystalline phase of the particles. The oxidation of titanium tetrachloride ($TiCl_4$) in a flame or oxygen plasma is a key route for the industrial manufacture of TiO_2 particles. Although the industrial manufacturing process is widely used, optimisation remains largely empirical. In many cases, the product is milled in order to control the final particle size distribution (PSD). This imposes an additional time and energy cost.

Detailed population balance models provide a tool to investigate how process conditions affect the particle properties [1, 2]. Such models are, within reason, able to include an arbitrarily detailed description of each particle. This facilitates the simulation of quantities that are directly comparable to experimental observations. Most importantly, it also enables the option to include key physical details in the model. For example, models where the particle growth is a function of the aggregate composition [3, 4], or, as is the case in this work, where sintering and neck growth are resolved on the basis of individual pairs of neighbouring particles [5, 6, 7].

Milling has been widely studied due to the high industrial demand for fine powders with tightly controlled properties. A lot of research has focused on identifying optimal milling parameters such as agitation speed, milling media size, filling ratio and suspension concentration. The effect of operational parameters on the milling performance of titanium dioxide has been investigated for fine grinding and dispersion of particles in wet stirred mills [8, 9, 10]. Other work has studied the substructure and mechanical properties of titania agglomerates [11], and the changes in fractal morphology of dense aggregates under wet milling [12].

Population balance models have also been used to characterise the milling process, and identify breakage mechanisms in wet stirred media milling [13, 14, 15, 16] by fitting Kapur's approximate first order solution [17] to experimental

data. More complex models consider non-linear effects and time-variant PBMs [18, 19].

Over long milling times and for sub-micron sized particles more complex phenomena are typically observed. This includes time delays in breakage [19], and grinding limits due to a minimum obtainable particle size and agglomeration effects [20, 10, 21, 16]. Modelling multimodal particle size distributions with statistical laws has been used as an alternative method for obtaining the grinding kinetics [9, 20].

The purpose of this paper is to develop a breakage model utilising the morphological data captured by a detailed particle model. This allows us to relate the reactor conditions during particle synthesis to the milling performance of TiO_2 particles. Particle synthesis is simulated using a detailed population balance model outlined in section 2 that describes the time evolution of the internal structure of the fractal aggregates. The simulation results are post-processed using a breakage model developed in section 3 to provide proof of concept that the morphological data in the detailed model can be related to milling behaviour. Five different breakage models are compared.

2. Computational details

A detailed population balance model coupled to a gas-phase kinetic model is used to simulate the synthesis of the TiO_2 particles. The kinetic model for the formation of TiO_2 particles from $TiCl_4$ is based on the mechanism proposed by West et al. [22]. It comprises 28 gas-phase species and 66 reactions. The dynamics of the population are described by the Smoluchowski coagulation equation with additional terms for particle inception, surface growth and sintering. The mathematical details of the model and methods are described in detail elsewhere [2], so only a brief summary is given here.

2.1. Particle model

The description of each aggregate in the population balance model (formally known as the type space) is illustrated in figure 1. Each aggregate is composed

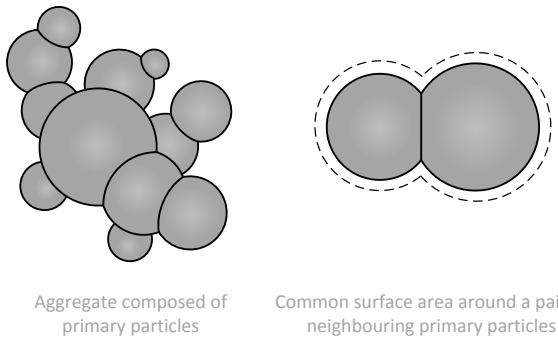

Figure 1: An illustration of the type space of the detailed particle model showing an aggregate particle composed of polydispersed primary particles (left panel). The level of sintering between primary particles is resolved by a common surface area (dashed line in right panel) for each pair of neighbouring primaries.

of primary particles, where neighbouring particles may be in point contact, fully coalesced or anywhere between. The model resolves the common surface area between each pair of neighbouring primary particles. The primary particle composition of an aggregate is polydispersed where each primary is described in terms of the number of TiO_2 units, from which the mass and volume are derived.

2.2. Particle processes

2.2.1. Inception

Inception, modelled as per Akroyd et al. [23], is assumed to be collision-limited and result from the bimolecular collision of gas-phase titanium oxychloride species

$$\begin{aligned} \mathrm{Ti}_{x_\alpha}\mathrm{O}_{y_\alpha}\mathrm{Cl}_{z_\alpha} + \mathrm{Ti}_{x_\beta}\mathrm{O}_{y_\beta}\mathrm{Cl}_{z_\beta} \longrightarrow \left(x_\alpha + x_\beta\right)\mathrm{TiO}_{2(\mathrm{s})} \\ + \left(\frac{y_\alpha + y_\beta}{2} - x_\alpha - x_\beta\right)\mathrm{O}_2 + \left(\frac{z_\alpha + z_\beta}{2}\right)\mathrm{Cl}_2, \quad x, y, z \geq 1, \end{aligned} \tag{1}$$

where the molecular collision diameter is taken as 0.65 nm [22]. An inception event creates a particle consisting of a single primary composed of $(x_\alpha + x_\beta)$ TiO_2 units.

2.2.2. Surface growth

Surface growth is treated as a single-step reaction as in Akroyd et al. [23]

$$\mathrm{TiCl_4 + O_2 \longrightarrow TiO_{2(s)} + 2\,Cl_2}, \tag{2}$$

with the rate expression

$$\frac{\mathrm{d}\big[\mathrm{TiO_2}\big]}{\mathrm{d}t} = k_\mathrm{s}\, A_\mathrm{s} \big[\mathrm{TiCl_4}\big]\big[\mathrm{O_2}\big], \tag{3}$$

where A_s is the surface area per unit volume of the TiO_2 population and k_s has an Arrhenius form

$$k_\mathrm{s} = A\ \exp\left(\frac{-E_\mathrm{a}}{RT}\right) \frac{\mathrm{m}}{\mathrm{s}} \cdot \frac{\mathrm{m}^3}{\mathrm{mol}}, \tag{4}$$

with activation energy E_a and pre-exponential factor A. One surface growth event adds one unit of TiO_2 to the particle. Equation (3) assumes fixed reaction orders with respect to $TiCl_4$ and O_2. Alternative models for the rate of surface growth are discussed by Shirley et al. [24].

2.2.3. Coagulation

An aggregate is formed when two particles stick together following a collision. The rate of collision is calculated using the transition regime coagulation kernel [25]

$$K_\mathrm{tr} = \left(\frac{1}{K_\mathrm{sf}} + \frac{1}{K_\mathrm{fm}}\right)^{-1}, \tag{5}$$

where the slip flow and free molecular kernels are

$$K_\mathrm{sf}(P_q, P_r) = \frac{2k_\mathrm{B}T}{3\mu}\left(\frac{1 + 1.257\mathrm{Kn}(P_q)}{d_c(P_q)} + \frac{1 + 1.257\mathrm{Kn}(P_r)}{d_c(P_r)}\right)(d_c(P_q) + d_c(P_r)), \tag{6}$$

and

$$K_\mathrm{fm}(P_q, P_r) = 2.2\sqrt{\frac{\pi k_\mathrm{B}T}{2}\left(\frac{1}{m(P_q)} + \frac{1}{m(P_r)}\right)}(d_c(P_q) + d_c(P_r))^2, \tag{7}$$

respectively. Kn is the Knudsen number

$$\mathrm{Kn}(P_q) = 4.74 \times 10^{-8}\frac{T}{p d_c(P_q)}, \tag{8}$$

m is the aggregate particle mass, d_c is the particle collision diameter, and μ is the viscosity of the gas-phase at pressure p and temperature T. After a coagulation

event, two primary particles (one from each coagulating particle) are assumed to be in point contact.

2.2.4. Sintering

Following the approach of Xiong and Pratsinis [26] and West et al. [22], sintering is modelled as occurring between neighbouring pairs of primary particles, where it is assumed that the common surface area C exponentially decays to the surface area of a mass-equivalent spherical particle, S_{sph},

$$\frac{\mathrm{d}C}{\mathrm{d}t} = -\frac{1}{\tau_{\mathrm{s}}}\left(C - S_{\mathrm{sph}}\right). \tag{9}$$

τ_{s} is a characteristic sintering time taken from Kobata et al. [27] as per West et al. [22]

$$\tau_{\mathrm{s}} = 7.4 \times 10^{16} T d_p^4 \exp\left(\frac{258000}{RT}\right), \tag{10}$$

where d_p is the diameter of the smaller primary. The sintering level of two primaries p_i and p_j is defined as per Shekar et al. [2],

$$s(p_i, p_j) = \frac{\frac{S_{\mathrm{sph}}(p_i,p_j)}{C} - 2^{-1/3}}{1 - 2^{-1/3}}. \tag{11}$$

Note that $0 \leq s(p_i, p_j) \leq 1$. Primaries are assumed to have coalesced if the sintering level exceeds 0.95. In this case the two primary particles merge into a single primary with the total TiO_2 composition of the original primaries.

2.3. Numerical method

The detailed population balance equations are solved using a stochastic numerical method [2]: a direct simulation algorithm with various enhancements to improve efficiency. The method uses a majorant kernel and fictitious jumps [28, 29, 25] to improve the computational speed of calculating the coagulation rate. A linear process deferment algorithm [30] is used to provide an efficient treatment of sintering and surface growth. Coupling of the particle model to the gas-phase chemistry, solved using an ODE solver, is achieved by an operator splitting technique [31].

3. Milling models

In the milling process, particles break due to stresses exerted by the milling media. Kwade and co-workers [32, 33] describe the process in terms of the frequency of stress events and the intensity of each stress event. The energy intensity is introduced as a key factor in determining whether a breakage event occurs. A stress event of sufficient intensity will result in breakage.

Low intensity shear stresses are sufficient for breaking weak agglomerates whereas higher intensity normal stresses are required to break crystalline material [34]. Normal stresses arise when a particle is caught in between milling beads during a collision. The resulting fragment size distribution is dependent on the properties of the material and the mode of fragmentation.

Three types of breakage mechanism are usually discussed in the literature: abrasion, cleavage and fracture [35, 13, 36, 37, 38, 19]. Abrasion involves a continuous loss of mass from the surface of a particle resulting in a bimodal fragment distribution. Cleavage produces fragments of the same order in size as the original particle while fracture results in disintegration of the particle into small fragments. The different modes of fragmentation often occur simultaneously during milling.

Epstein [39] first introduced population balance equations to the study of milling, modelling breakage as two successive operations represented by a selection and a breakage function. The selection function is the probability of a particle of given size breaking and is usually observed to increase with particle size [37]. The breakage function describes the shape of the fragment size distribution and is characterised by the fragmentation mechanism.

The idea of this work is to explore whether the information in the type space of the detailed population balance model can be related to the observed milling performance of TiO_2 particles. The particle breakage rate and fragment distribution are determined by a breakage model that utilises the morphological information captured by the detailed particle model.

Figure 2 shows a sketch of a milling curve. The average particle size is

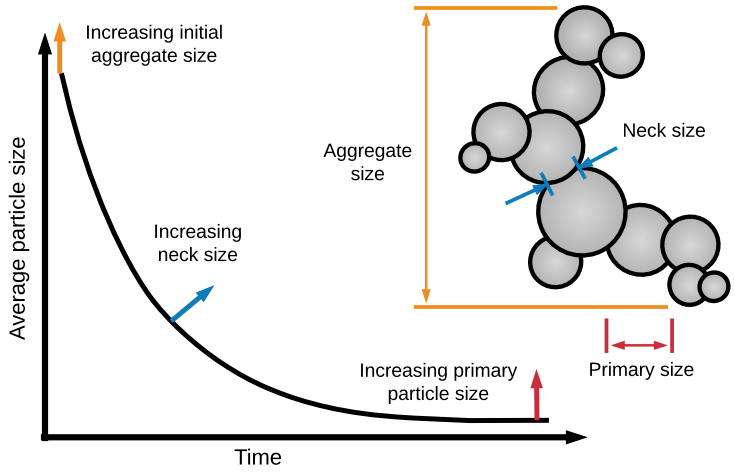

Figure 2: A sketched milling curve and a possible concept relating the detailed particle type space to the shape of the curve. The coloured arrows indicate a possible influence of a particle property on the shape of the milling curve.

observed to decrease during the initial part of the milling curve. Eventually the system reaches an asymptotic state where no further significant decrease is observed.

One possible concept relating the detailed particle model to the milling curve is shown overlaying figure 2. The average particle size is obtained from the aggregate size distribution and the asymptotic particle size is a function of the primary particle size distribution. The slope of the milling curve depends on the breakage mechanism and is some function of the aggregate particle structure. Breakage, assumed to occur at the necks between neighbouring primaries, is related to the neck size distribution and the fractal geometry of the particle. The particle geometry is responsible for transmitting milling stresses to necks and the neck strength is related to the neck size.

In this work, we apply a milling model based on algorithm 1 as a post-process to the detailed population balance model. The particle breakage rate is given by the breakage models discussed in section 3.2. Two of the breakage models utilise a neck radius to characterise how strongly neighbouring primaries are

connected. The neck model is discussed in the next section.

3.1. Neck size calculation

A neck between two primary particles is modelled as overlapping spheres as shown in figure 3. The neck size can be calculated from the common surface area C_{ij} and spherical-equivalent radii r_i and r_j of each primary particle.

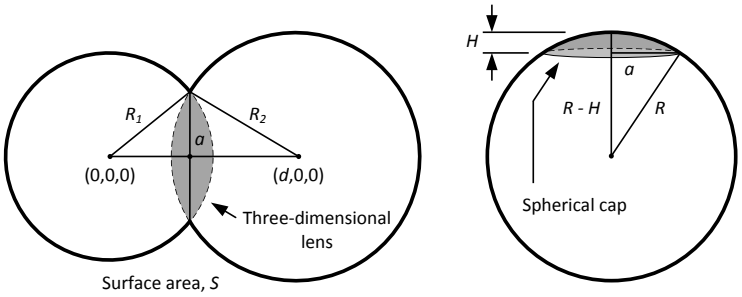

Figure 3: Geometry of the neck between two primary particles.

The volume V and surface area S of two overlapping spheres are given

$$V\left(R_1,R_2,d\right)=\frac{4\pi}{3}\Big(R_1^3+R_2^3\Big) - \frac{\pi}{12d}\Big(R_1+R_2-d\Big)^2\Big(d^2+2R_1d+2R_2d-3R_1^2-3R_2^2+6R_1R_2\Big), \tag{12}$$

and

$$S\left(R_1,R_2,d\right)=4\pi\Big(R_1^2+R_2^2\Big)-\pi\Big(a^2+H_1^2\Big)-\pi\Big(a^2+H_2^2\Big), \tag{13}$$

where a is the radius of the neck [40]

$$a\left(R_1,R_2,d\right)= \frac{1}{2d}\Big[\left(R_1+R_2+d\right)\left(R_1+R_2-d\right)\left(-R_1+R_2-d\right)\left(R_1-R_2-d\right)\Big]^{\frac{1}{2}}, \tag{14}$$

and where H_1 and H_2 are the heights of the spherical caps

$$H_i=R_i-R_i\cos\left(\arcsin\left(\frac{a}{R_i}\right)\right),$$

and R_1 and R_2 are the radii of two spheres whose centres are separated by a distance $d\in[0,R_1+R_2]$. The final term in equation (12) is the volume of the

Algorithm 1: Milling algorithm applied as a post-process to the detailed particle model.

Input: Initial state of the particle ensemble at time t_0; Final time t_{stop}.

Output: State of the particle ensemble at final time t_{stop}.

$t \leftarrow t_0$.

while $t < t_{\text{stop}}$ **do**

Calculate the rate, $\rho_{\text{part}}(P_q)$, for each aggregate particle P_q,

$$\rho_{\text{part}}(P_q) = \sum_{i<j} \rho_{ij},$$

where ρ_{ij} is the breakage rate for the neck between two primaries p_i and p_j.

Calculate the total rate, ρ_{total}, for all N particles,

$$\rho_{\text{total}} = \sum_{q=1}^{N} \rho_{\text{part}}(P_q).$$

Calculate an exponentially distributed waiting time Δt with parameter ρ_{total},

$$\Delta t = \frac{-\ln(X)}{\rho_{\text{total}}},$$

where X is a uniform random variate in the interval $[0, 1]$.

With probability $\rho_{\text{part}}(P_q)/\rho_{\text{total}}$ select a particle P_q.

With probability $\rho_{ij}/\rho_{\text{part}}(P_q)$ select a neck.

Break the neck between primaries p_i and p_j, and update the particle ensemble:

$$P_q \rightarrow P_r + P_s,$$
$$N \leftarrow N + 1.$$

Increment $t \leftarrow t + \Delta t$.

end

three-dimensional lens [40] and the final terms in equation (13) are the areas of each spherical cap [41] created by the intersection of the spheres.

Under the assumption that the volume of the three-dimensional lens is evenly redistributed over the surface of the particles in an even layer of thickness Δr, the radii of each sphere in figure 3 can be written in terms of the spherical-equivalent radii of the corresponding primary particles

$$R_i = r_i + \Delta r. \tag{15}$$

Equations (12) and (13) may be reduced to two equations in two unknowns using the substitutions in equations (14) and (15),

$$V(\Delta r, d) = v(p_i) + v(p_j),$$
$$S(\Delta r, d) = C_{ij},$$

and can be solved for the values of Δr and d, and hence the radius of the neck $a_{ij}(\Delta r, d)$ for each pair of neighbouring primary particles with corresponding total volume $v(p_i) + v(p_j)$ and common surface area C_{ij}.

3.2. Breakage models

Figure 4 illustrates a single breakage event where an aggregate particle P_q fragments into two smaller daughter particles P_r and P_s. Breakage is treated as binary and always occurs at a neck connecting two neighbouring primary particles. Individual primaries are assumed not to break.

An aggregate particle is modelled as two arms extending from a neck as depicted by the dashed arrows in figure 4. Note that this representation can be applied to any chosen neck within the aggregate. The composition of the arms is equivalent to that of the two daughter fragments formed in the event of breakage. When a particle is caught in a three-body collision with two milling beads the stresses are transmitted by these arms to the neck. The neck that breaks during such a collision will depend on a number of factors including the neck size or strength, and the size, shape and orientation of the respective arms.

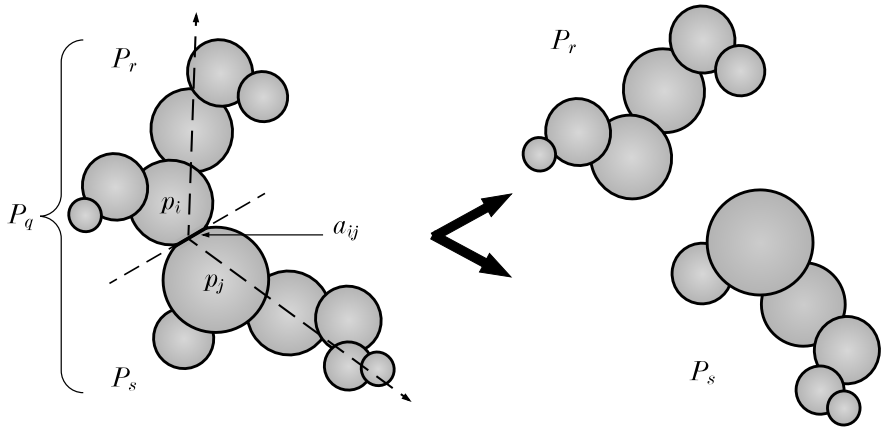

Figure 4: A breakage event. An aggregate particle P_q fragments into two daughter particles P_r and P_s at a neck of radius a_{ij} connecting two primaries p_i and p_j. The aggregate is represented as two arms, corresponding to the respective daughter particles, extending from the neck.

The rate of breakage of a neck between two primaries p_i and p_j is expressed as a function of the neck and daughter particle (fragment) properties

$$\rho_{ij} = \rho_{ij}(P_r(..., p_i, ..., \mathbf{C}_r), P_s(..., p_j, ..., \mathbf{C}_s), a_{ij}), \tag{16}$$

where $P_r(..., p_i, ..., \mathbf{C}_r)$ and $P_s(..., p_j, ..., \mathbf{C}_s)$ are the daughter particles formed in the breakage event, a_{ij} is the neck radius, and $\mathbf{C}$ is the respective connectivity matrix storing the common surface areas as defined in Shekar et al. [2]. Five different breakage models are discussed below. It is assumed that a rate constant k captures the operational parameters of the mill and that the mill is capable of producing collisions of sufficient intensity to break all particle necks. The total particle breakage rate for a particle P_q is

$$\rho_{\text{part}}(P_q) = \sum_{i<j} \rho_{ij}, \tag{17}$$

where we sum over $i < j$ to avoid double counting.

3.2.1. Simple neck model

The breakage rate is assumed to be only a function of the neck radius, calculated as per section 3.1

$$\rho_{ij} = k a_{ij}^{\alpha}, \tag{18}$$

for constants k and α.

3.2.2. Total mass model

The probability of breakage is typically observed to increase with particle size. In this model we assume that the rate of breakage for a neck is proportional to the sum of daughter fragment masses $m(P_r)$ and $m(P_s)$ or equivalently, the total particle mass $m(P_q)$

$$\rho_{ij} = k(m(P_r(..., p_i, ..., \mathbf{C}_r)) + m(P_s(..., p_j, ..., \mathbf{C}_s))) \tag{19}$$

$$= k m(P_q(..., p_i, p_j, ..., \mathbf{C}_q)), \tag{20}$$

for constant k. Breakage is equally likely for every neck in an aggregate. The rate of breakage for a single aggregate particle is therefore a function of its total mass and the number of necks.

$$\rho_{\text{part}}(P_q) = k(n_{\text{p}}(P_q) - 1) m(P_q), \tag{21}$$

where $n_{\text{p}}(P_q)$ is the number of primaries and $(n_{\text{p}}(P_q) - 1)$ corresponds to the number of necks, which is always one less than the number of primaries.

3.2.3. Fragment mass model

A simple way to characterise the size of a fragment arm is by its mass. More massive arms are expected to apply greater stresses on a neck due to greater leverage and arms of similar mass will maximise the applied stress. This is modelled by setting the rate of breakage proportional to the product of the daughter particle masses

$$\rho_{ij} = k \cdot m(P_r(..., p_i, ..., \mathbf{C}_r)) \cdot m(P_s(..., p_j, ..., \mathbf{C}_s)), \tag{22}$$

for a constant k and where $m(P_r)$ and $m(P_s)$ are the masses of the two particle fragments joined at the neck between primaries p_i and p_j.

3.2.4. Fragment radius model

A better measure of the size of a fragment arm is its radius of gyration, which accounts for the fractal structure of the aggregate,

$$R_{\mathrm{g}} = \overline{d_{\mathrm{p}}} \left(\frac{n_{\mathrm{p}}}{k_{\mathrm{f}}} \right)^{1/D_{\mathrm{f}}}. \tag{23}$$

n_{p} is the number of primaries, $\overline{d_{\mathrm{p}}}$ is the average primary diameter, D_{f} is the fractal dimension, and k_{f} is the fractal prefactor. A typical value of 1.8 is assumed for the fractal dimension [42]. Using the same form for the rate as in equation (22) the breakage rate for a single neck is

$$\rho_{ij} = k \cdot R_{\mathrm{g}}(P_r(..., p_i, ..., \mathbf{C}_r)) \cdot R_{\mathrm{g}}(P_s(..., p_j, ..., \mathbf{C}_s)), \tag{24}$$

for a constant k and where $R_{\mathrm{g}}(P_r)$ and $R_{\mathrm{g}}(P_s)$ correspond to the radii of gyration of the two arms extending from the neck between primaries p_i and p_j.

3.2.5. Fragment and neck radius model

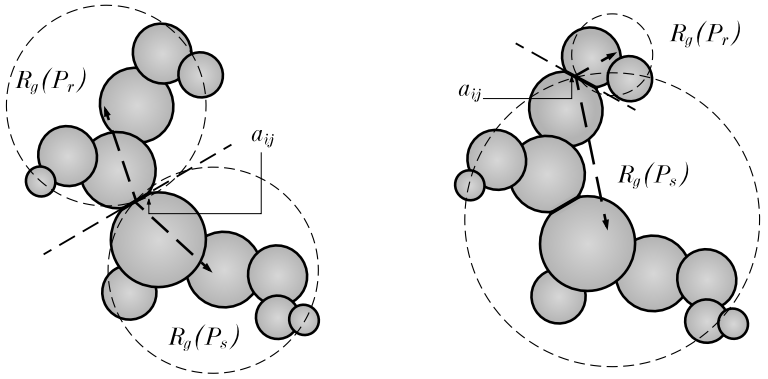

(a) (b)

Figure 5: Two possible breakage events. The selected neck between primaries p_i and p_j is indicated by a dashed line and the fragment arms extending from the neck have radii of gyration $R_{\mathrm{g}}(P_r)$ and $R_{\mathrm{g}}(P_s)$. Symmetrical breakage in subfigure (a) produces daughter fragments with similar radii of gyration while subfigure (b) shows an asymmetrical breakage event.

The fragment radius of gyration model in section 3.2.4 assumes that all necks are equally strong. However, the degree of sintering between primary particles will effect the breakage rate. By combining the fragment radius model (section 3.2.4) and the simple neck model (section 3.2.1) we can relate the breakage rate to both the geometry of the aggregate particle and the size of the neck. The rate of breakage is

$$\rho_{ij} = k \cdot R_{\mathrm{g}}(P_r(..., p_i, ..., \mathbf{C}_r)) \cdot R_{\mathrm{g}}(P_s(..., p_j, ..., \mathbf{C}_s)) \cdot a_{ij}^{\alpha}, \tag{25}$$

for constants k and α.

Figure 5 illustrates two possible breakage events. We expect that breakage is most likely if both radii of gyration are large and of similar magnitude as shown in figure 5(a). However, in the case of a very weak neck an asymmetrical abrasion-like event is also possible as depicted in figure 5(b).

4. Results and discussion

4.1. Hot wall reactor simulations

To produce particles for post-processing with the milling models we simulated the hot wall reactor experiment of Pratsinis et al. [43], fitting the surface growth rate for the detailed particle model. The original investigation measured the reaction of 5:1 (mol/mol) O_2:$TiCl_4$ in argon (99% by volume) in a 1/8-in-I.D. tube heated to 973-1273 K.

Pratsinis et al. [43] estimate an effective rate constant for the overall oxidation kinetics of $TiCl_4$ vapour

$$k_{\mathrm{eff}} = -\frac{\ln(C_{\mathrm{o}}/C_{\mathrm{i}})}{t}, \tag{26}$$

assuming the reaction is first-order in $TiCl_4$ with Arrhenius kinetics and where C_{i} and C_{o} are the measured inlet and outlet $TiCl_4$ concentrations. t is the residence time in the isothermal zone of the reactor held at temperature T. The experiment was simulated using the imposed temperature profile of Pratsinis et al. [43, Fig. 3] modelled by Akroyd et al. [23]. The temperature starts at

300 K and rises to the isothermal zone temperature T remaining there for the residence time t. At the end of the isothermal zone the temperature falls back to 300 K and remains at this temperature until the end of the simulation.

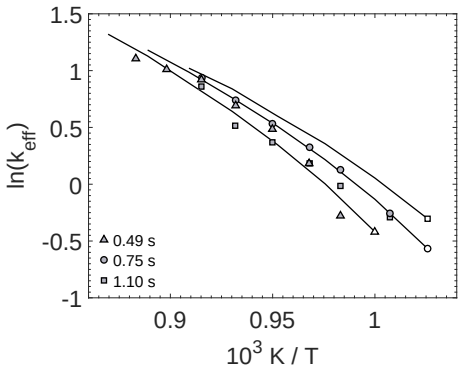

Figure 6: Arrhenius plot of the oxidation rate of $TiCl_4$ at three different residence times. Black lines terminating in open symbols: fitted simulation results (4 runs with 8192 particles); Shaded symbols: Experimental data [43, Fig. 4].

Figure 6 shows good agreement between detailed particle model simulations with 8192 stochastic particles and the experimental results of Pratsinis et al. [43, Fig. 4]. The data are presented in the original form for ease of comparison. A reaction that is overall first order in $TiCl_4$ would produce a single straight line through all residence times. The differences observed between the simulation results for the different isothermal residence times suggests a reaction that is close to but not exactly first order overall.

The surface growth rate was fitted with activation energy $E_a = 60$ kJ/mol and pre-exponential factor $A = 1340$ m^4/(s $\cdot$ mol) (see equation (4)). The fitted activation energy is in agreement with the theoretically calculated value (55$\pm$25 kJ/mol) of Shirley et al. [24].

Simulation data is visualised in figure 7 in the form of TEM style images showing titania particles produced in the hot wall reactor under two different isothermal zone residence times and temperatures. The examples presented in the figure are for two extremes within the simulated range of reactor conditions

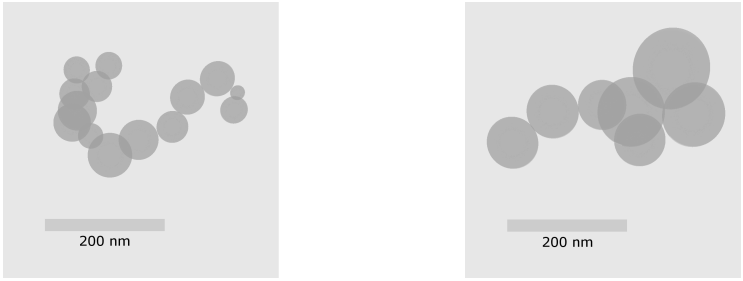

(a) 0.49 s at 1000 K (b) 1.1 s at 1100 K

Figure 7: TEM style images of titania aggregates produced in the simulated hot wall reactor under different conditions. The visualisation does not depict the level of sintering between particles, however this information is captured by the model.

showing the greatest difference in particle morphology.

Aggregate particles produced over a longer isothermal residence time at higher temperature (1.1 s at 1100 K shown in figure 7(b)) are composed of a smaller number of larger primaries than aggregates produced at a lower temperature and shorter isothermal residence time (0.49 s at 1000 K shown in figure 7(a)). This is clear from the primary diameter distribution (figure 8) and the distribution of the number of primaries per aggregate (figure 9).

The difference in aggregate particle size is less pronounced. Figure 10 shows the distribution of particle collision diameters calculated as per Lavvas et al. [44]. The aggregate particle size is a function of the number of primary particles, their respective diameters, and the level of sintering between neighbours. This allows for aggregates of comparable size despite the different primary particle properties. The largest particles are of similar size under both sets of reactor conditions, but the distribution in figure 10(a) extends to smaller collision diameters. The smallest particles are composed of a single primary particle and the lower minimum value arises due to the smaller mean primary diameter.

Figure 11 shows the distribution of neck radii for the two cases. The distributions are truncated at 0.3 nm: of the order of the rutile unit cell size. Below this size, a second peak was observed in both simulations at a radius of 0.01–0.1

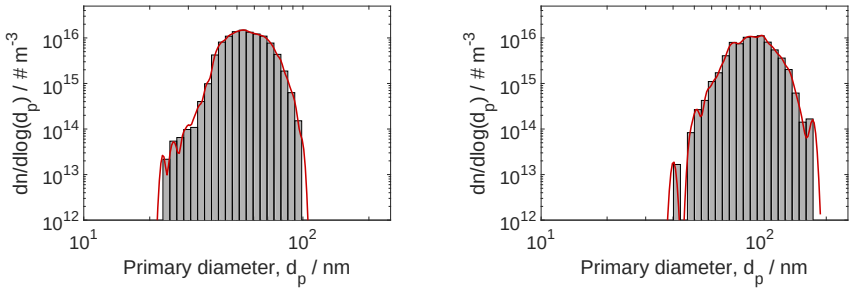

(a) 0.49 s at 1000 K

(b) 1.1 s at 1100 K

Figure 8: Primary particle diameter distributions produced under different simulated isothermal zone residence times and temperatures. The red line shows the Gaussian kernel density estimate.

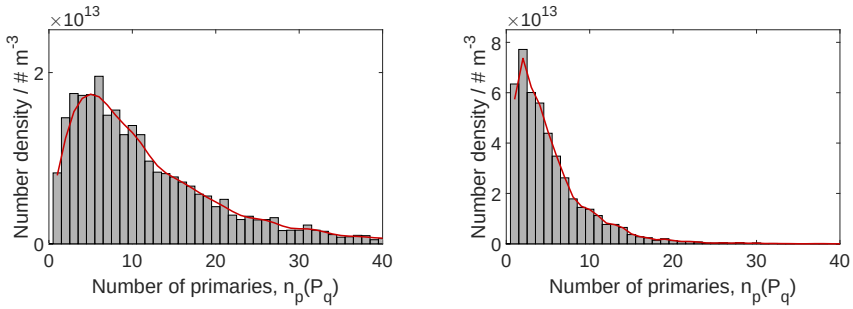

(a) 0.49 s at 1000 K

(b) 1.1 s at 1100 K

Figure 9: Distribution of the number of primaries per titania aggregate produced under different simulated isothermal zone residence times and temperatures. The red line shows the Gaussian kernel density estimate.

nm: smaller than an atomic diameter. The overlapping spheres model permits the neck radius to take any positive value and does not account for quantization at very small length scales. Furthermore, molecular dynamics studies of sintering of nanometre sized titania particles show that the formation of an initial neck is very rapid, of the order of 10 picoseconds [45, 46, 47], whereas in this work sintering is treated as a continuous process with the same characteristic time at all stages.

The bimodal distribution arises due to the simulated temperature profile in

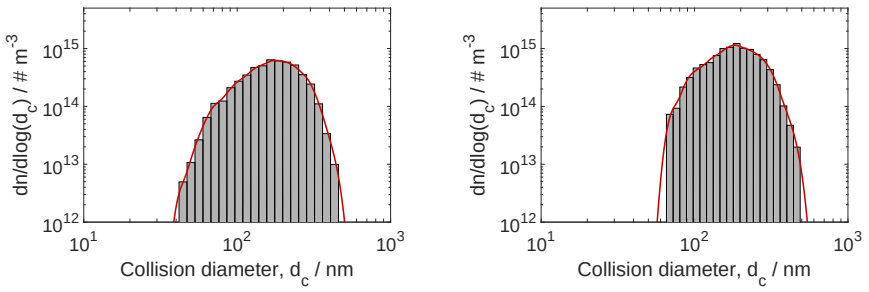

(a) 0.49 s at 1000 K

(b) 1.1 s at 1100 K

Figure 10: Collision diameter distributions of titania aggregates produced under different simulated isothermal zone residence times and temperatures. The red line shows the Gaussian kernel density estimate.

which the temperature falls to 300 K at the end of the isothermal zone. The stronger temperature dependence of sintering causes the sintering process to slow faster than coagulation resulting in the formation of small necks. The 0.49 s isothermal zone residence time simulations spent a longer time at 300 K than the 1.1 s simulations which created a larger number of small necks.

Up to 5% of necks were calculated to be in point contact ($a_{ij} = 0$). These necks are considered to represent primaries bound by weak dispersion forces that have yet to begin sintering. Larger necks with well defined radii correspond to sintered primaries joined by strong chemical bonds.

4.2. Comparison of breakage models

The breakage models presented in section 3.2 were used to post-process the hot wall reactor simulation results of section 4.1 using algorithm 1. The results of post-processing the 0.49 s at 1000 K simulation are discussed here as a representative case because they display the general features of the different breakage models also observed in the other reactor simulations. Under the assumption that necks in point contact ($a_{ij} = 0$) break apart easily we processed the data to break these necks prior to milling.

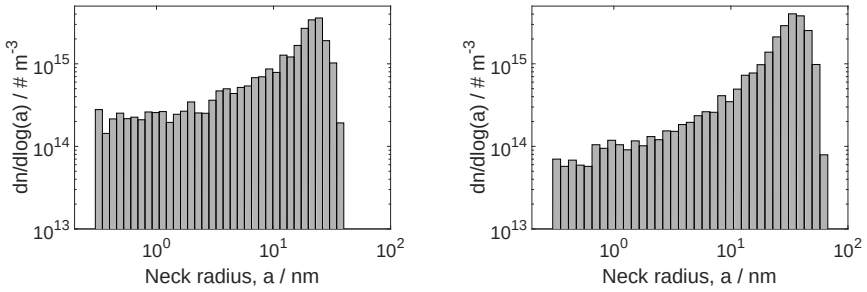

(a) 0.49 s at 1000 K (b) 1.1 s at 1100 K

Figure 11: Neck radius distribution for titania aggregates produced in the simulated hot wall reactor under two different conditions. Necks smaller than 0.3 nm are not shown.

4.2.1. Milling curves

Typically observed industrial milling curves (from Huntsman Pigments and Additives) are shown in figure 12. The volume weighted mean particle size is observed to decrease logarithmically over the period covered by the data. The width of the PSD as measured by the volume weighted geometric standard deviation (GSD) of particle size also exhibits logarithmic decay. The data set does not contain the initial particle size distribution nor the long time behaviour of particles under milling.

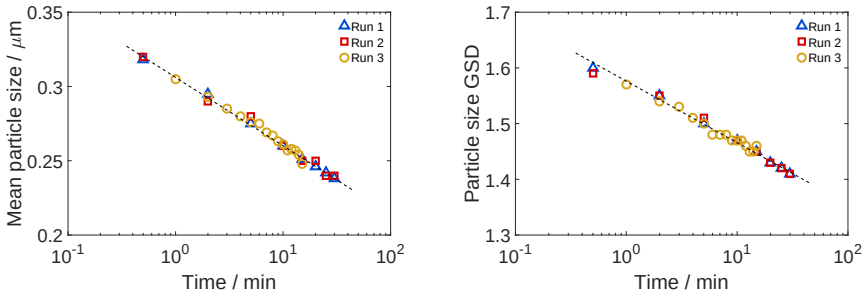

(a) Mean particle size (b) Geometric standard deviation

Figure 12: Experimental milling curves (Huntsman Pigments and Additives) show logarithmic decay in both the volume weighted mean particle size and geometric standard deviation. Dashed line added to guide the eye.

Figure 13 shows the corresponding simulated milling curves for the different breakage models. The time coordinate is non-dimensionalised by defining a characteristic time equal to the time taken for the mass weighted geometric mean collision diameter to fall to 90% of its initial value. The mass weighted geometric mean (GM) and mass weighted GSD are given by

$$\ln(\mathrm{GM}) = \frac{\sum_{q=1}^{N} m(P_q) \ln(d_\mathrm{c}(P_q))}{\sum_{q=1}^{N} m(P_q)}, \tag{27}$$

$$\ln(\mathrm{GSD}) = \sqrt{\frac{\sum_{q=1}^{N} m(P_q) \left[\ln(d_\mathrm{c}(P_q)) - \ln(\mathrm{GM})\right]^2}{\sum_{q=1}^{N} m(P_q)}}, \tag{28}$$

for N particles P_q each with mass $m(P_q)$ and collision diameter $d_\mathrm{c}(P_q)$.

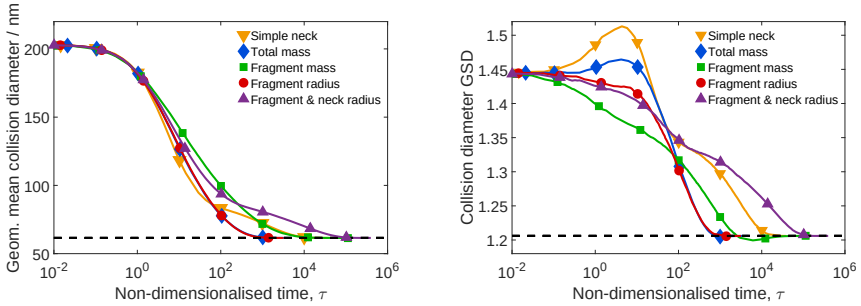

(a) (b)

Figure 13: Milling curves for different breakage models obtained by post-processing hot wall reactor simulation results for the 0.49 s at 1000 K case. (a) shows the mass weighted geometric mean collision diameter and (b) the mass weighted geometric standard deviation in the collision diameter. The horizontal dashed line indicates the asymptotic value calculated from the primary particle distribution.

A value of -1 was selected for the exponent α in the simple neck and the fragment radius and neck models yielding rates inversely proportional to the neck radius. A negative exponent implies that larger necks require greater stresses to break. More negative choices of α introduce a long intermediate period during which the GM and GSD change very little. This is observed to small degree in the simple neck model ($\alpha = -1$ case) in figure 13(b) where the gradient changes at around $\tau = 100$.

Figure 13(a) plots the mass weighted geometric mean collision diameter against non-dimensionalised time. All models exhibit an intermediate period of approximately logarithmic decay as seen in the experimental milling curves (figure 12). The total mass and fragment radius models have almost identical mean collision diameter curves. The simple neck and fragment and neck radius models show two distinct phases of size reduction characterised by different gradients. The change in gradient arises due to the bimodal nature of the neck size distribution. The first mode of small necks breaks first followed by the second mode of larger and stronger necks.

The GSD curves (figure 13(b)) offer a clearer way to differentiate between models. Most display an intermediate period of approximately logarithmic decay. An interesting feature is the initial increase in GSD seen in the total mass and simple neck models. Such an increase in the variance has been observed experimentally in the grinding of titanium dioxide [9]. This arises due to the formation of small fragments that cause a widening in the particle size distribution and can be seen in the mass weighted collision diameter distributions in figure 14. The distribution near the maximum GSD for the simple neck model ($\tau = 4.4$ in figure 14(a)) is skewed with more mass density at smaller diameters contributing to a wider, lower peak. In comparison, the fragment and neck radius model in figure 14(b) maintains a more symmetric distribution due to a preference for symmetrical breakage events.

4.2.2. Comparison to a first order model

There are uncertainties around modelling the milling process, therefore models are fitted to experimental data in order to extract the milling kinetics and identify the breakage mechanism at work. The milling process can be described with a PBM and the size reduction behaviour is often adequately approximated by a first order exponential function over sufficiently short milling times [48, 49, 15, 16]. In this section we want to explore how the kinetics of our breakage models compare with a first order exponential model.

The cumulative form of the discrete population balance equation for batch

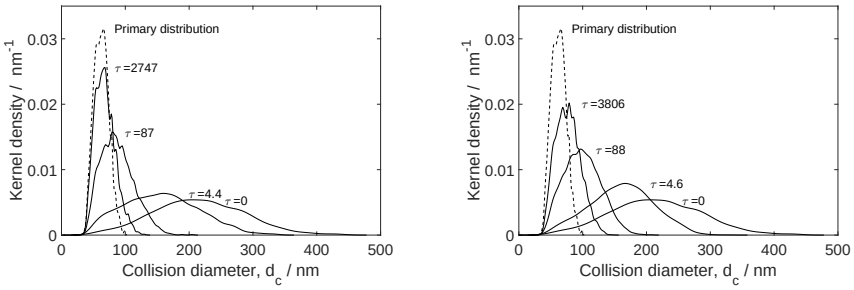

(a) Simple neck model (b) Fragment and neck radius model

Figure 14: Mass weighted collision diameter distributions generated using a Gaussian kernel density estimate at different non-dimensionalised times for the 0.49 s at 1000 K reactor simulation post-processed with the (a) simple neck and (b) fragment and neck radius models.

milling is (following [48, 14])

$$\frac{\mathrm{d}R_i}{\mathrm{d}t} = -S_i R_i(t) + \sum_{j=1}^{i-1} (S_{j+1} B_{i,j+1} - S_j B_{i,j}) R_j(t), \tag{29}$$

with

$$R_i(t) = \sum_{j=1}^{i} w_j(t) \qquad \text{and} \qquad B_{i,j} = \sum_{k=i+1}^{n} b_{k,j}. \tag{30}$$

$R_i(t)$ is the cumulative oversize mass fraction of particles larger than size x_i. w_j is the mass fraction of particles in size class j, with w_1 corresponding to the largest size class. S_i, the selection function, is the probability of breakage of particles in size class i. $b_{k,j}$, the breakage function, is the mass fraction of particles in class j that break to produce particles in size class k.

The approximate solution of Kapur [17], to first order in t, has the form

$$R_i(t) = R_i(0) \exp\left(G_i t\right). \tag{31}$$

and the selection function S_i can then be related to G_i [14]

$$S_i = -G_i. \tag{32}$$

Figure 15 presents the simulation results in the form $R_i(\tau)/R_i(0)$ for nine size classes. The particle size, x_i, is the spherical equivalent diameter. The

breakage models all display an early period of exponential decay consistent with a first order solution. Exponential curves with parameter G_i (equation (31)) were fitted to the simulation data in this period and are shown in figure 15 as dashed lines.

After the initial period of approximately exponential decay the curves begin to diverge. An approximate first order solution is therefore only appropriate over a short milling time up to $\tau = 1$ to $\tau = 5$, depending on the model. However, we can compare the fitted values of G_i as a function of spherical equivalent diameter x_i, valid over the initial period, to typical selection functions reported in the literature.

The function G_i can often be represented by a power law in particle size [48, 50]

$$G_i = -ax_i^b. \tag{33}$$

Values of the exponent b observed for the milling of solid particles are typically close to unity [50, 48, 16]. A quadratic form for G_i has been reported for the milling of micrometer sized titanium dioxide [20]. Significantly larger values of b have been observed for alumina particles sintered at 1873 K (about 3) [50] and for the grinding of amorphous pre-mullite powder (3.18) [51]. Hennart et al. [16] show a power law dependence with exponent 6.5 for particles below 0.180 μm in diameter when grinding a crystalline organic product limited by aggregation phenomena.

Figure 16 shows a power law fitting for the fitted values of G_i for the different models. The exponent ranges from 3.37 for the simple neck model to 7 in the case of the fragment mass model. These are considerably larger than typically observed values for grinding and closer to values reported for highly sintered aggregates and small particles approaching a grinding limit.

4.2.3. Choice of breakage model

While it is difficult to exclude models based on the qualitative comparison of milling curves, the current work illustrates the different features produced by each model, particularly with regard to the GSD and evolution of the PSD. Of

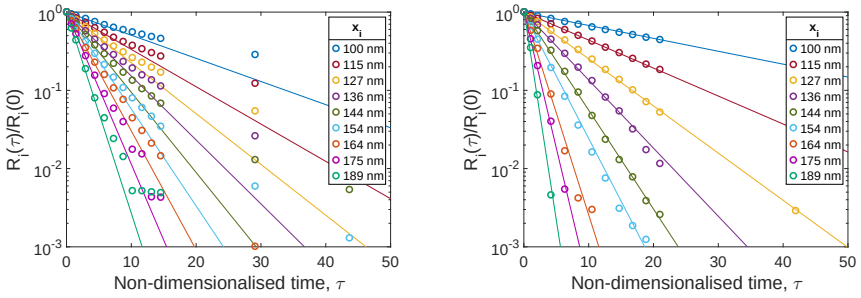

(a) Simple neck model

(b) Total mass model

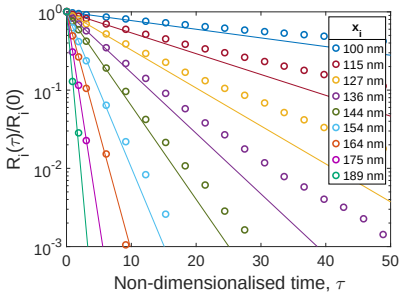

(c) Fragment mass model

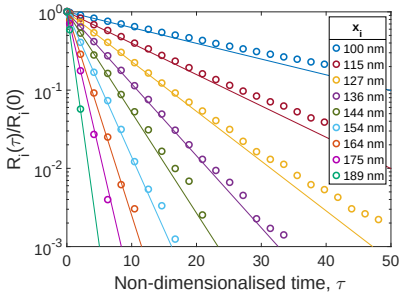

(d) Fragment radius model

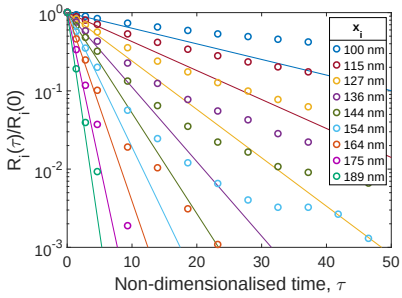

(e) Fragment and neck radius model

Figure 15: Normalised cumulative mass fraction oversize against non-dimensionalised time for nine spherical equivalent particle diameters up to time $\tau = 50$. Symbols: simulation data; Lines: exponential decay fitted to data at early times.

the five breakage models discussed here only the fragment and neck radius model considers the aggregate particle geometry as well as the neck strength. The dependence on aggregate geometry favours symmetrical breakage in a cleavage

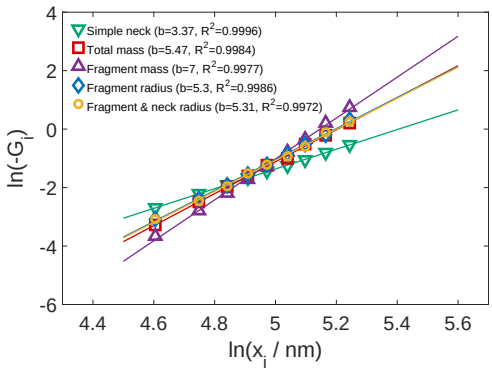

Figure 16: Fitted power law in spherical equivalent particle diameter for the different breakage models. Symbols: G_i fitted to data in figure 15; Lines: fitted power law. The fitted exponent b and R^2 value are shown in the legend.

type mechanism. On the other hand, the neck size dependence favours small necks allowing for cases of asymmetrical breakage near the particle extremities similar to an abrasion mechanism. Since the model accounts for the detailed particle morphology it serves as good candidate for further study.

4.3. Effect of reactor conditions on milling curves

The fragment and neck radius model was applied to simulations of the hot wall reactor experiment under different conditions. Results are shown in figure 17. The time coordinate was non-dimensionalised for all cases using the characteristic time calculated for the 0.49 s at 1000 K case allowing for better comparison along the time axis.

All simulations take approximately the same time to reach an asymptotic state. Two phases of approximately logarithmic decay, characterised by different gradients, are observed due to the bimodal neck size distribution. In the 1.1 s isothermal zone residence time simulations the first phase is not as well defined. The longer isothermal residence time results show a slower decrease in the mean particle size and a smaller total change. Both 0.49 s simulations display a rapid first phase of size reduction followed by a slower second phase.

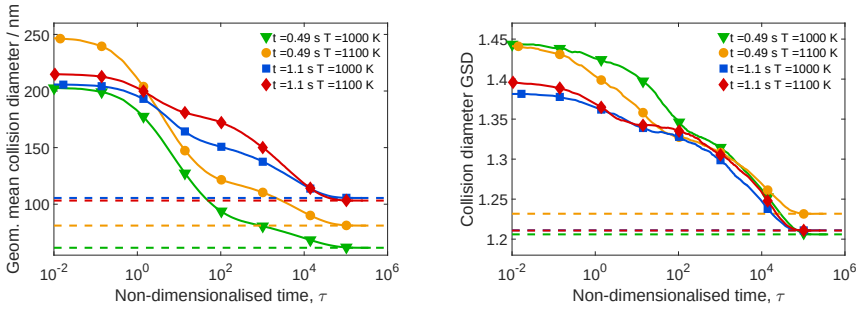

(a) Mean particle collision diameter (b) Geometric standard deviation

Figure 17: Milling curves for the fragment and neck radius model obtained by post-processing hot wall reactor simulation results under different conditions. The horizontal dashed lines show the asymptotic values calculated from the primary particle distributions.

This model shows that particles synthesised over a short residence time in the high temperature isothermal zone of the reactor are milled faster and reduced to a smaller asymptotic size. The GSD has a higher initial value but catches up with the longer isothermal zone residence time simulations over the first phase of size reduction. The effect of temperature, within the range used in this study, is less pronounced.

5. Conclusions

A detailed population balance was used to model the formation of titanium dioxide particles in a hot wall reactor and validated against the experiment of Pratsinis et al. [43]. The detailed particle type space was shown to resolve morphological differences between particles produced under different reactor conditions.

Breakage models were developed that utilise the information captured by the detailed particle model and used as a post-process to simulate the milling of TiO_2 particles produced in the hot wall reactor simulations. The milling curves exhibited features consistent with experimental observations. The chosen breakage model accounts for the fractal structure of the aggregate particles as well as the size of necks between neighbouring primaries. Application of

this milling model to particles produced under different residence times and temperatures showed that the model is sensitive to the reactor conditions under which the TiO_2 particles were synthesised.

Further work is needed to compare the model against experimental results and fit the breakage rate constant. This would first require simulation of the reactor conditions under which the experimental TiO_2 particles are produced to allow subsequent comparison to experimental milling data. There is also scope to improve the sintering and neck size models given the observed limitations of the current model at low levels of sintering.

Acknowledgements

This project is partly funded by the National Research Foundation (NRF), Prime Minister's Office, Singapore under its Campus for Research Excellence and Technological Enterprise (CREATE) programme. The authors would like to thank Huntsman Pigments and Additives for financial support.

References

[1] Shekar S, Smith AJ, Menz WJ, Sander M, Kraft M. A multidimensional population balance model to describe the aerosol synthesis of silica nanoparticles. J Aerosol Sci 2012;44:83–98. doi:10.1016/j.jaerosci.2011.09.004.

[2] Shekar S, Menz WJ, Smith AJ, Kraft M, Wagner W. On a multivariate population balance model to describe the structure and composition of silica nanoparticles. Comput Chem Eng 2012;43:130–47. doi:10.1016/j.compchemeng.2012.04.010.

[3] Celnik M, Raj A, West R, Patterson R, Kraft M. Aromatic site description of soot particles. Combust Flame 2008;155:161–80. doi:10.1016/j.combustflame.2008.04.011.

[4] Celnik MS, Sander M, Raj A, West RH, Kraft M. Modelling soot formation in a premixed flame using an aromatic-site soot model and an improved oxidation rate. Proc Combust Inst 2009;32:639–46. doi:10.1016/j.proci.2008.06.062.

[5] Morgan NM, A.Patterson RI, Kraft M. Modes of neck growth in nanoparticle aggregates. Combust Flame 2008;152:272–5. doi:10.1016/j.combustflame.2007.08.007.

[6] Sander M, West RH, Celnik MS, Kraft M. A detailed model for the sintering of polydispersed nanoparticle agglomerates. Aerosol Sci Technol 2009;43:978–89. doi:10.1080/02786820903092416.

[7] Sander M, Patterson RIA, Braumann A, Raj A, Kraft M. Developing the PAH-PP soot particle model using process informatics and uncertainty propagation. Proc Combust Inst 2011;33:675–83. doi:10.1016/j.proci.2010.06.156.

[8] Ohenoja K, Illikainen M, Niinimäki J. Effect of operational parameters and stress energies on the particle size distribution of TiO_2 pigment in stirred media milling. Powder Technol 2013;234:91–6. doi:10.1016/j.powtec.2012.09.038.

[9] Bel Fadhel H, Frances C, Mamourian A. Investigations on ultra-fine grinding of titanium dioxide in a stirred media mill. Powder Technol 1999;105:362–73. doi:10.1016/S0032-5910(99)00160-6.

[10] Inkyo M, Tahara T, Iwaki T, Iskandar F, Hogan Jr. CJ, Okuyama K. Experimental investigation of nanoparticle dispersion by beads milling with centrifugal bead separation. J Colloid Interface Sci 2006;304:535–40. doi:10.1016/j.jcis.2006.09.021.

[11] Gesenhues U. Substructure of titanium dioxide agglomerates from dry ball-milling experiments. J Nanopart Res 1999;1:223–34. doi:10.1023/A:1010097429732.

[12] Jeon S, Thajudeen T, Jr. CJH. Evaluation of nanoparticle aggregate morphology during wet milling. Powder Technol 2015;272:75 – 84. doi:http://dx.doi.org/10.1016/j.powtec.2014.11.039.

[13] Varinot C, Hiltgun S, Pons MN, Dodds J. Identification of the fragmentation mechanisms in wet-phase fine grinding in a stirred bead mill. Chem Eng Sci 1997;52:3605–12. doi:10.1016/S0009-2509(97)89693-5.

[14] Berthiaux H, Varinot C, Dodds J. Approximate calculation of breakage parameters from batch grinding tests. Chem Eng Sci 1996;51:4509–16. doi:10.1016/0009-2509(96)00275-8.

[15] Hennart SLA, Wildeboer WJ, van Hee P, Meesters GMH. Identification of the grinding mechanisms and their origin in a stirred ball mill using population balances. Chem Eng Sci 2009;64:4123–30. doi:10.1016/j.ces.2009.06.031.

[16] Hennart SLA, van Hee P, Drouet V, Domingues MC, Wildeboer WJ, Meesters GMH. Characterization and modeling of a sub-micron milling process limited by agglomeration phenomena. Chem Eng Sci 2012;71:484–95. doi:10.1016/j.ces.2011.11.010.

[17] Kapur PC. Kinetics of batch grinding. Part B: An approximate solution to the grinding equation. Trans AIME 1970;247:309–13.

[18] Bilgili E, Scarlett B. Population balance modeling of non-linear effects in milling processes. Powder Technol 2005;153:59–71. doi:10.1016/j.powtec.2005.02.005.

[19] Bilgili E, Hamey R, Scarlett B. Nano-milling of pigment agglomerates using a wet stirred media mill: Elucidation of the kinetics and breakage mechanisms. Chem Eng Sci 2006;61:149–57. doi:10.1016/j.ces.2004.11.063.

[20] Frances C. On modelling of submicronic wet milling processes in bead mills. Powder Technol 2004;143-144:253–63. doi:10.1016/j.powtec.2004.04.018.

[21] Sommer M, Stenger F, Peukert W, Wagner NJ. Agglomeration and breakage of nanoparticles in stirred media mills – a comparison of different methods and models. Chem Eng Sci 2006;61:135–48. doi:10.1016/j.ces.2004.12.057.

[22] West RH, Shirley RA, Kraft M, Goldsmith CF, Green WH. A detailed kinetic model for combustion synthesis of titania from $TiCl_4$. Combust Flame 2009;156:1764–70. doi:10.1016/j.combustflame.2009.04.011.

[23] Akroyd J, Smith AJ, Shirley R, McGlashan LR, Kraft M. A coupled CFD-population balance approach for nanoparticle synthesis in turbulent reacting flows. Chem Eng Sci 2011;66:3792–805. doi:10.1016/j.ces.2011.05.006.

[24] Shirley R, Akroyd J, Miller LA, Inderwildi OR, Riedel U, Kraft M. Theoretical insights into the surface growth of rutile TiO_2. Combust Flame 2011;158:1868–76. doi:10.1016/j.combustflame.2011.06.007.

[25] Patterson RIA, Singh J, Balthasar M, Kraft M, Wagner W. Extending stochastic soot simulation to higher pressures. Combust Flame 2006;145:638–42. doi:10.1016/j.combustflame.2006.02.005.

[26] Xiong Y, Pratsinis SE. Formation of agglomerate particles by coagulation and sintering—Part I. A two-dimensional solution of the population balance equation. J Aerosol Sci 1993;24:283–300. doi:10.1016/0021-8502(93)90003-R.

[27] Kobata A, Kusakabe K, Morooka S. Growth and transformation of TiO_2 crystallites in aerosol reactor. AIChE J 1991;37:347–59. doi:10.1002/aic.690370305.

[28] Eibeck A, Wagner W. An efficient stochastic algorithm for studying coagulation dynamics and gelation phenomena. SIAM J Sci Comput 2000;22:802–21. doi:10.1137/S1064827599353488.

[29] Goodson M, Kraft M. An efficient stochastic algorithm for simulating nanoparticle dynamics. J Comput Phys 2002;183:210–32. doi:10.1006/jcph.2002.7192.

[30] Patterson RIA, Singh J, Balthasar M, Kraft M, Norris JR. The linear process deferment algorithm: A new technique for solving population balance equations. SIAM J Sci Comput 2006;28:303–20. doi:10.1137/040618953.

[31] Celnik M, Patterson R, Kraft M, Wagner W. Coupling a stochastic soot population balance to gas-phase chemistry using operator splitting. Combust Flame 2007;148:158–76. doi:10.1016/j.combustflame.2006.10.007.

[32] Kwade A, Blecher L, Schwedes J. Motion and stress intensity of grinding beads in a stirred media mill. Part 2: Stress intensity and its effect on comminution. Powder Technol 1996;86:69–76. doi:10.1016/0032-5910(95)03039-5.

[33] Kwade A. Wet comminution in stirred media mills – research and its practical application. Powder Technol 1999;105:14–20. doi:10.1016/S0032-5910(99)00113-8.

[34] Kwade A, Schwedes J. Breaking characteristics of different materials and their effect on stress intensity and stress number in stirred media mills. Powder Technol 2002;122:109–21. doi:10.1016/S0032-5910(01)00406-5.

[35] Redner S. Fragmentation. In: Herrmann HJ, Roux S, editors. Statistical models for the fracture of disordered media. Amsterdam: Elsevier; 1990, p. 321–48. doi:10.1016/B978-0-444-88551-7.50021-5.

[36] Hogg R. Breakage mechanisms and mill performance in ultrafine grinding. Powder Technol 1999;105:135–40. doi:10.1016/S0032-5910(99)00128-X.

[37] Hogg R, Cho H. A review of breakage behavior in fine grinding by stirred-media milling. KONA Powder Part J 2000;18:9–19. doi:10.14356/kona.2000007.

[38] Bel Fadhel H, Frances C. Wet batch grinding of alumina hydrate in a stirred bead mill. Powder Technol 2001;119:257–68. doi:10.1016/S0032-5910(01)00266-2.

[39] Epstein B. Logarithmico-normal distribution in breakage of solids. Ind Eng Chem 1948;40:2289–91. doi:10.1021/ie50468a014.

[40] Weisstein EW. Sphere-sphere intersection. From MathWorld - A Wolfram Web Resource; accessed 15 Oct 2015. URL: http://mathworld.wolfram.com/Sphere-SphereIntersection.html.

[41] Weisstein EW. Spherical cap. From MathWorld - A Wolfram Web Resource; accessed 15 Oct 2015. URL: http://mathworld.wolfram.com/SphericalCap.html.

[42] Tsantilis S, Kammler HK, Pratsinis SE. Population balance modeling of flame synthesis of titania nanoparticles. Chem Eng Sci 2002;57:2139–56. doi:10.1016/S0009-2509(02)00107-0.

[43] Pratsinis SE, Bai H, Biswas P, Frenklach M, Mastrangelo SVR. Kinetics of titanium (IV) chloride oxidation. J Am Ceram Soc 1990;73:2158–62. doi:10.1111/j.1151-2916.1990.tb05295.x.

[44] Lavvas P, Sander M, Kraft M, Imanaka H. Surface chemistry and particle shape. Processes for the evolution of aerosols in Titan's atmosphere. Astrophys J 2011;728:80. doi:10.1088/0004-637X/728/2/80.

[45] Buesser B, Gröhn AJ, Pratsinis SE. Sintering rate and mechanism of TiO_2 nanoparticles by molecular dynamics. J Phys Chem C 2011;115:11030–5. doi:10.1021/jp2032302.

[46] Collins DR, Smith W, Harrison NM, Forester TR. Molecular dynamics study of the high temperature fusion of TiO_2 nanoclusters. J Mater Chem 1997;7:2543–6. doi:10.1039/A704673A.

[47] Koparde VN, Cummings PT. Molecular dynamics simulation of titanium dioxide nanoparticle sintering. J Phys Chem B 2005;109:24280–7. doi:10.1021/jp054667p.

[48] Berthiaux H, Heitzmann D, Dodds JA. Validation of a model of a stirred bead mill by comparing results obtained in batch and continuous mode grinding. Int J Miner Process 1996;44-45:653–61. doi:10.1016/0301-7516(95)00073-9.

[49] Varinot C, Berthiaux H, Dodds J. Prediction of the product size distribution in associations of stirred bead mills. Powder Technol 1999;105:228–36. doi:10.1016/S0032-5910(99)00142-4.

[50] Hogg R, Dynys AJ, Cho H. Fine grinding of aggregated powders. Powder Technol 2002;122:122–8. doi:10.1016/S0032-5910(01)00407-7.

[51] Matijašić G, Kurajica S. Grinding kinetics of amorphous powder obtained by sol-gel process. Powder Technol 2010;197:165–9. doi:10.1016/j.powtec.2009.09.010.